Autonomous rigid-wing sailboats—Force balances for monitoring sailing performance

Matias Waller [1,2], Ulysse Dhomé [3], Jakob Kuttenkeuler [3] and Andy Ruina [4]

October 5, 2021

Abstract

Real-time monitoring and evaluation of practical trials with autonomous sailboats is often challenging: varying winds and waves influence a visual evaluation directly connected to a subjective verification of expected mechanical behavior while the inherent nature of sailing with different sensors operating in different coordinates complicates an objective data-based evaluation. In this paper, we illustrate the use of force balances as a tool for monitoring performance and detecting unreliable sensors. Differences in perspectives between on-board performance monitoring on the one hand and mission planning on the other hand and corresponding coordinates and definitions of angles are treated in detail. In addition, it is shown how the model can be used for fault detection and as a basis for a framework for quantifying and assessing model development.

Keywords: Autonomous sailboat; wingsail; model-based data evaluation; fault detection; force balance

1 Introduction

Projects with autonomous rigid-wing sailboats often involve a range of practical challenges including design and construction of wingsails and electronic systems for sensors and control. Consequently, practical trials are used for, among other things, verifying mechanical behavior, control robustness and performance, sensor reliability, etc. Furthermore, projects typically rely on engaged students and can form part of exam requirements with a related emphasis on different aspects of the operation. As is often the case with projects of similar nature, deadline for meeting exam requirements approaches during practical experiments and, accordingly, time for more extensive quantitative reflection and possibilities for repeated trials might be limited. For the long-term goal of releasing a fleet of small autonomous sailboats for collecting data over long time-periods in waters with significant currents, uncertainties in expected sailing performance are important to consider for successful planning of missions. In this paper, we introduce a tool that combines computational power with basic sailing theory and that can readily be used for sailing performance evaluation. Given the array of institutions involved in robotic sailing, one of our goals is to illustrate the basics of sailing without assuming any prior knowledge. For this reason, the basic model is kept simple, e.g., two-dimensional with no need for CFD simulations, but still comprehensive enough to capture, and with the computational approach illustrates, the essence of sailing theory in a few pages. In detail, we also discuss differences in perspectives between on-shore planning and design on the one side, and on-board evaluation on the other. Furthermore, our basic steady-state model is evaluated by computational means on data from two rigid-wing sailing robots and our approach is found to predict sailing speed with reasonable accuracy. Encouraged by the evaluation, we propose different possibilities for further use of our tool using the basic model:

- sailing performance monitoring,
- sensor fault detection,
- quantifying and illustrating possibilities for performance improvement by design choices.
- quantifying and illustrating possibilities for model improvement.

The study is limited to rigid wingsails for five reasons. Firstly, we have access to data from two different sailing robots with rigid wings. Secondly, data-collecting missions with autonomous rigid wing sailing robots have apparently been very successful, see, e.g., the survey in [9]. Thirdly, great advances in high-performing sailing have been achieved with wingsails during the last decades. Fourthly, the use of rigid wingsails seems to be a promising alternative in the search for zero-omission commercial shipping [1]. Lastly, the aerodynamics for rigid wings are hopefully more well-defined than for soft sails and experiments should, accordingly, be more repeatable.

The theoretical basis for our model and all subsequent analysis is the balance of aerodynamic and hydrodynamic forces at equilibrium, i.e.,

when speed and direction of boat, wind and any possible currents can be approximated as constant. This basic model is presented next.

2 Basic model

For clarity of presentation and, as is common in the literature, the forces acting on the sailboat are divided into aerodynamic and hydrodynamic forces. For our analysis and a general understanding of sailing and the basic model, some central variables are summarized in Table 1.

physical quantity	symbol	unit
heading	θ	degrees
course (over water)	ϑ	degrees
leeway	$\lambda = \theta - \vartheta$	degrees
boat speed (over water)	v_b	m/s
apparent wind angle	β_{AWA}	degrees
apparent wind speed	v_{AW}	m/s
angle of attack (wingsail)	α	degrees
true wind angle	β_{TWA}	degrees
true wind speed	v_{TW}	m/s
water current angle	φ	degrees
water current speed	v_s	m/s

Table 1: Central variables considered in the study.

In the literature, there is variation regarding the interpretation of some of these variables and, in addition, the definition of apparent wind angle warrants some discussion. In this paper, the following definitions are used.

1. Heading θ: the direction of the longitudinal axis of the boat in earth frame. Ideally, a measure of heading will be provided by the compass (or the gyro).
2. Course over water ϑ: the direction of the movement of the boat relative to water in earth frame. In the absence of currents, i.e., $v_s = 0$, this will be the same as course over ground provided by the (D)GPS.
3. Leeway λ: the difference between heading and course over water. This will also be the angle of attack for the keel. A negative leeway will indicate a course over water to port. Leeway λ is illustrated in Fig. 1.
4. Boat speed over water v_b: the speed of the boat relative to the water. In the absence of currents, this will be the same as speed over ground provided by the (D)GPS. Note that this includes speed in the direction of the heading (sometimes called surge) as well as side speed (sway). Boat velocity $\vec{v}_b$ is illustrated in Fig. 1.
5. Apparent wind angle β_{AWA}: The angle of the wind relative to the heading of the boat as it is perceived on the boat. It can be noted

that apparent wind angle often is defined relative to the course over water and *not* heading. The reason for defining the angle relative to the heading is the sailing robot point of view: typically, the apparent wind angle is measured by a wind vane physically installed relative to the heading of the boat. By convention, 0 to 180° indicates starboard and 0 to -180° port.

For some discussions, e.g., the course theorem and the boat polar, it is more suitable to define wind angles relative to the course over water and for this purpose $\beta_{\mathrm{AWA},\lambda} = \beta_{\mathrm{AWA}} + \lambda$ is also used. The angle β_{AWA} is illustrated in Fig. 1.

6. Apparent wind speed v_{AW}: The speed of the wind relative to the boat, i.e., the speed as it is perceived on the boat. Typically measured by an anemometer. Apparent wind velocity $\vec{v}_{\mathrm{AW}}$ is illustrated in Fig. 1.
7. True wind angle β_{TWA}: The angle of the wind relative to the heading of the boat as it is perceived when stationary on the water.

   Again, true wind angle is often defined relative to the movement of the boat instead, i.e., course over ground in the absence of currents and for some discussions $\beta_{\mathrm{TWA},\lambda} = \beta_{\mathrm{TWA}} + \lambda$ is accordingly used. The angle $\beta_{\mathrm{TWA},\lambda}$ is illustrated in Fig. 1.
8. True wind speed v_{TW}: The speed of the wind as it is perceived when stationary on the water. True wind velocity $\vec{v}_{\mathrm{TW}}$ is illustrated in Fig. 1.

In addition, apparent and true wind *direction*, i.e., the angles in earth frame, β_{AWD} and β_{TWD} are also used. Next, the aerodynamic force is presented followed by the hydrodynamic force.

2.1 Aerodynamic force

The aerodynamic force, $\vec{F}_a$, is the result of a (symmetric) wingsail set at an angle of attack towards the apparent wind. It is decomposed into lift, $\vec{F}_{l,a}$, perpendicular to the apparent wind, and drag, $\vec{F}_{d,a}$, in the direction of the apparent wind as illustrated in Fig. 2. It is assumed that the (signed) magnitudes of lift and drag can be calculated by standard expressions for airfoils, i.e.,

$$F_{l,a} = \frac{1}{2}\rho_a C_l A_s v_{\mathrm{AW}}^2 \tag{1}$$

and

$$F_{d,a} = \frac{1}{2}\rho_a C_d A_s v_{\mathrm{AW}}^2 \tag{2}$$

where ρ_a is the density of air and A_s is the wingsail area. The coefficients for lift and drag, C_l and C_d, will primarily depend on the profile of the wing and the angle of attack and, to some extent, on v_{AW}. For the two profiles, NACA0012 and the NACA0018, experimental results for C_l and C_d as a function of angle of attack are illustrated in Fig. 3.

The reason for choosing these profiles is due to the wingsails and keels for the two autonomous sailing robots used for evaluating the model. The sailing robots are ASPire, depicted in Fig. 16 and described in, e.g., [4],

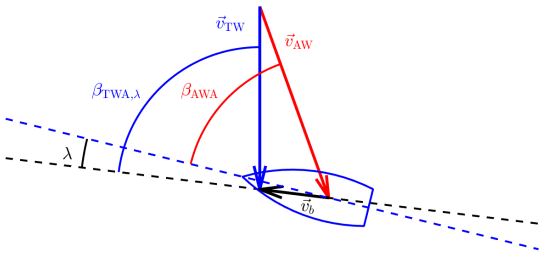

Figure 1: Sailing velocity triangle: true wind $\vec{v}_{\mathrm{TW}}$ (blue), apparent wind $\vec{v}_{\mathrm{AW}}$ (red) and boat velocity $\vec{v}_b$ (black). Angles: true wind angle with respect to the movement of the boat $\beta_{\mathrm{TWA},\lambda}$ (blue), apparent wind angle with respect to the heading of the boat β_{AWA} (red), and leeway λ (black). The dashed blue line represents the heading of the boat and the dashed black line illustrates the actual movement of the boat. Boat illustrated as a solid blue line. For illustrative purposes, leeway has been exaggerated.

and Maribot Vane depicted in the same figure and described in, e.g., [2]. The ASPire and Maribot Vane have similar hulls based on the International 2.4mR sailing class. The profile for the keel was chosen as NACA0012 based on a 3-D scan of the hull of Maribot Vane. For Maribot Vane, the wingsail is based on the NACA0018 profile while ASPire uses two sides of the asymmetrical NACA63_2-618 to make it symmetrical. For simplicity, NACA0018 is still used for all calculations for both wingsails. Apart from the size of the wingsails, which is smaller on ASPire, the models for the two sailing robots are thus identical.

In the figure, the coefficients for the two profiles are illustrated at different Reynolds numbers. The Reynolds number is defined by $\mathrm{Re} = vL/\mu$, where μ is the dynamic viscosity of the surrounding fluid, v is the speed of the surrounding fluid, and L is a characteristic dimension, i.e., the chord length for foils. For ASPire and Maribot Vane, the value $\mathrm{Re} = 360000$ corresponds to a wind speed of approximately $6 - 7$ m/s while $\mathrm{Re} = 1000000$ corresponds to a water speed of approximately 1.5 m/s. In order to calculate lift and drag for the wingsail in general, the only measurements needed are thus apparent wind speed and the angle of attack for the wingsail.

Wingsails often operate at quite small angles of attack in order to avoid the stalling region. Typically, leeway is also often small. In such cases, a common approach is to use a linear model for C_l and possibly quadratic for C_d. In the current paper, however, we are also interested in exploring the model for a large angle of attack or leeway. Therefore, realistic values for C_l and C_d at large angles of attack are needed and the

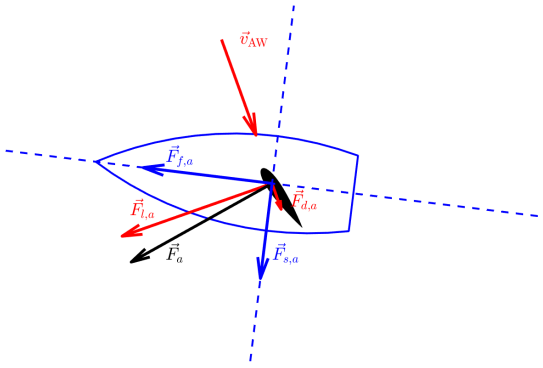

Figure 2: Apparent wind velocity (red), $\vec{v}_{\mathrm{AW}}$, acting on a wingsail (black solid) to give the aerodynamic force, $\vec{F}_a$ (black) that can be decomposed in lift (red), $\vec{F}_{l,a}$, perpendicular to the apparent wind, and drag (red), $\vec{F}_{d,a}$, in the direction of the apparent wind. Forward projection (blue), $\vec{F}_{f,a}$, in the direction of the heading of the boat, and a side force (blue), $\vec{F}_{s,a}$, perpendicular to the forward force are included. Boat illustrated as a solid blue line.

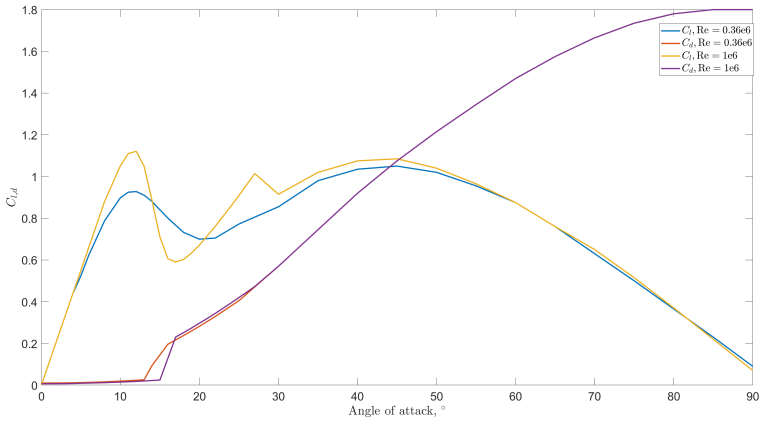

Figure 3: C_l and C_d as a function of angle of attack ($C_l(-x) = -C_l(x)$ and $C_l(-x) = C_d(x)$) for the two different profiles, NACA0012 and NACA0018. NACA0018 at Re = 360000 and for NACA0012 at Re = 1000000. Experimental data presented in [8].

simplified models are not sufficient for all of the applications considered in this paper. In addition, induced drag and reduced lift is included by

the approximations

$$C_d = C_d + \frac{C_l^2}{0.7\pi A_R} \tag{3}$$

$$C_l = C_l - \frac{C_l^2}{0.7\pi A_R} \tag{4}$$

where A_R is the aspect ratio, i.e., the span (height) of the wing divided by the chord. Next, the hydrodynamic force is presented

2.2 Hydrodynamic force

Similarly to the aerodynamic force, the hydrodynamic force, $\vec{F}_h$, can also be decomposed into lift and drag, $F_{l,h}$ and $F_{d,h}$ and these are illustrated in Fig. 4. These are assumed to be given by

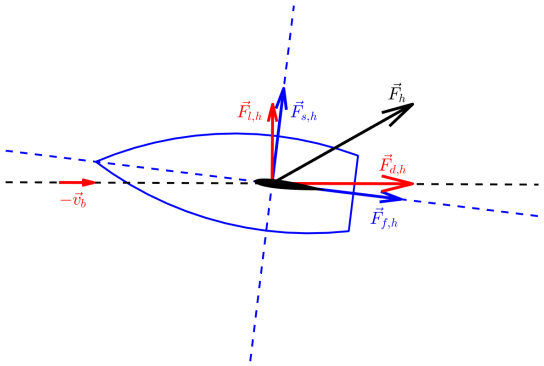

Figure 4: Boat velocity results in movement through water respresented by negative boat velocity, $-\vec{v}_b$ (red), acting on the keel (black solid) to give the hydrodynamic force, $\vec{F}_h$ (black) that can be decomposed in lift, $\vec{F}_{l,h}$ (red) perpendicular to the movement through water, and drag, $\vec{F}_{d,h}$ (red) in the direction of the movement through water. Forward projection, $\vec{F}_{f,h}$ (blue) in the direction of the heading of the boat, and a side force, $\vec{F}_{s,h}$ (blue) perpendicular to the forward force are included. Boat illustrated as a solid blue line.

$$F_{l,h} = \frac{1}{2}\rho_w C_{l,k} A_k v_b^2 \tag{5}$$

perpendicular to the movement through water and

$$F_{d,h} = F_{\text{wave}} + \frac{1}{2}\rho_w (C_R A_w + C_{d,k} A_k) v_b^2 \tag{6}$$

in the direction of the movement through water. Note that due to leeway, this direction does not correspond to the heading of the boat. The density of water is ρ_w, v_b is boat speed through water, $C_{l,k}$ and $C_{d,k}$ are the

coefficients for lift and drag for the keel, A_k is the keel surface area, A_w is the wetted area of the hull, C_R is a skin friction coefficient and F_{wave} is wave resistance due to the waves *generated* by the boat when moving through water (and not due to external waves).

While C_R and F_{wave} certainly are a result of movement through water only, it is unclear whether experimental results summarized in, e.g., [3] include a projection in the heading of the boat or not. For high-performing sailboats and commercial vessels, this distinction might be negligible, but can be significant for small sailing boats operating at low speeds and possibly in waters with significant currents. If a projection in the heading is included, the terms F_{wave} and $F_{\text{sf}} = \frac{1}{2}\rho_w C_R A_w v_b^2$ should be moved to Eq. (10). For now, the terms are included above and C_R and F_{wave} are estimated based on v_b and geometric details for the hull and follows the presentation in [3]. These empirical equations are

$$C_R = \frac{0.075}{(\log_{10}(588000 L_{\text{WL}} v_b) - 2)^2}; \tag{7}$$

where L_{WL} is the length of the waterline in m. For F_{wave} is given by

$$F_{\text{wave}} = V_C \rho_w g \left(a_0 + \left(a_1 \frac{L_{\text{CB}}}{L_{\text{WL}}} + a_2 C_P + a_3 \frac{V_C^{(2/3)}}{A_{\text{WP}}} + a_4 \frac{B_{\text{WL}}}{L_{\text{WL}}} + a_5 \frac{L_{\text{CB}}}{L_{\text{CF}}} + a_6 \frac{B_{\text{WL}}}{H_{\text{BWL}}} + a_7 C_M \right) \frac{V_C^{(1/3)}}{L_{\text{WL}}} \right) \tag{8}$$

In the equation, V_C is the canoe body volume, L_{CB} the longitudinal centre of buoyancy from the forward perpendicular, C_P the prismatic coefficient, $C_P = V_S/(A_M L_{\text{WL}})$ where V_S is the submerged volume, A_M the maximum cross-sectional area, A_{WP} the waterplane area, B_{WL} the maximum waterline beam, L_{CF} the longitudinal centre of flotation from the forward perpendicular, H_{BWL} the height of submerged area at B_{WL} excluding appendages, e.g., keel and rudder, and, finally, $C_M = A_M/(B_{\text{WL}} H_{\text{BWL}})$ is the midship section coefficient. The parameters a_i are functions of the Froude number, $\text{Fr} = \frac{v_b}{\sqrt{g L_{\text{WL}}}}$, and are provided in Table 2.

Table 2: Coefficients a_i of Eq. (8) as a function of the Froude number.

Fr	a_0	a_1	a_2	a_3	a_4	a_5	a_6	a_7
0	0	0	0	0	0	0	0	0
0.1500	-0.0005	0.0023	-0.0086	-0.0015	0.0061	0.0010	0.0001	0.0052
0.2000	-0.0003	0.0059	-0.0064	0.0070	0.0014	0.0013	0.0005	-0.0020
0.2500	-0.0002	-0.0156	0.0031	-0.0021	-0.0070	0.0148	0.0010	-0.0043
0.3000	-0.0009	0.0016	0.0337	-0.0285	-0.0367	0.0218	0.0015	-0.0172
0.3500	-0.0026	-0.0567	0.0446	-0.1091	-0.0707	0.0914	0.0021	-0.0078
0.4000	-0.0064	-0.4034	-0.1250	0.0273	-0.1341	0.3578	0.0045	0.1115
0.4500	-0.0218	-0.5261	-0.2945	0.2485	-0.2428	0.6293	0.0081	0.2086
0.5000	-0.0388	-0.5986	-0.3038	0.6033	-0.0430	0.8332	0.0106	0.1336
0.5500	-0.0347	-0.4764	-0.2361	0.8762	0.4219	0.8990	0.0096	-0.2272
0.6000	-0.0361	0.0037	-0.2960	0.9661	0.6123	0.7534	0.0100	-0.3352
0.6500	0.0008	0.3728	-0.3667	1.3957	1.0343	0.3230	0.0072	-0.4632
0.7000	0.0108	-0.1238	-0.2026	1.1282	1.1836	0.4973	0.0038	-0.4477
0.7500	0.1023	0.7726	0.5040	1.7867	2.1934	-1.5479	-0.0115	-0.0977

From Eq.-(8) it is not obvious how wave-generating drag depends on the velocity of the boat v_b. Therefore, the different hydrodynamic drag forces as a function of v_b are illustrated in Fig. 5 for the case of $\lambda = 1^\circ$

and using the hull-characteristics for ASPire and Maribot Vane. As the figure reveals, F_{wave} is negligible for small v_b, but dominates when v_b exceeds 2.2 m/s, effectively limiting the top speed. This characteristic of F_{wave} is the obvious reason for the necessity of lifting the hulls out of the water for top-performing sailing vessels seen in, e.g., America's Cup. The non-smoothness of F_{wave} in the figure is due to linear interpolation when determining the values for a_i in Table 2 as a function of v_b.

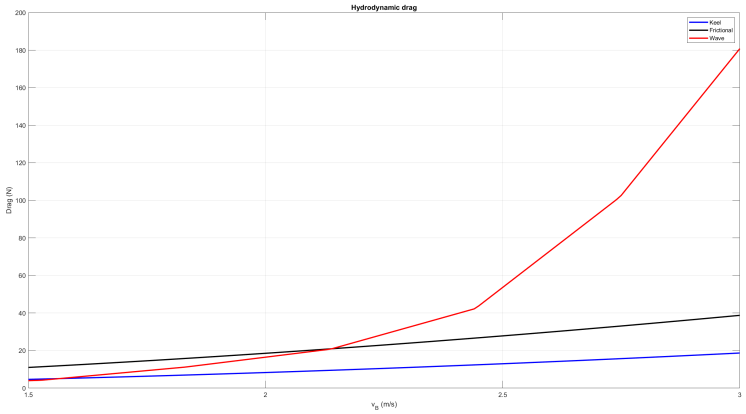

Figure 5: Hydrodynamic drag as a function of v_b with $\lambda = 1°$. $F_{d,\text{keel}} = \frac{1}{2}\rho_w C_{d,k} A_k v_b^2$, $F_{\text{sf}} = \frac{1}{2}\rho_w C_R A_w v_b^2$ and F_{wave} given by Eq. (8).

For calculating hydrodynamic lift and drag, $F_{l,h}$ and $F_{d,h}$, the measurements needed are boat speed (through water) and leeway. In the case of no currents, i.e., surrounding water is stationary relative to earth, measurements are typically provided by the (D)GPS for speed over ground (taken as boat speed v_b) and leeway as the difference between heading, θ, and course over ground provided by (D)GPS (taken as course over water, ϑ. This gives leeway, $\lambda = \theta - \vartheta$, i.e., the underwater angle of attack for the keel central for estimating $C_{l,k}$ and $C_{d,k}$.

Next, the aerodynamic and hydrodynamic forces are considered in the same frame of reference.

2.3 Side and forward forces

For an improved understanding of the relevant on-boat coordinates, i.e., a measurement point of view, the aerodynamic and hydrodynamic forces can be considered in the same frame of reference. Given an apparent wind angle, heading and course according to previous definitions, the aerodynamic and hydrodynamic lift and drag can be projected in a forward force, $\vec{F}_f$, in the direction of the heading of the boat, and a side force, $\vec{F}_s$, perpendicular to the forward force. The corresponding (signed) magnitudes

are given by

$$\begin{aligned} F_{f,a} &= \text{sgn}(\beta_{\text{AWA}})\sin(\beta_{\text{AWA}})F_{l,a} - \cos(\beta_{\text{AWA}})F_{d,a} \\ F_{s,a} &= -\left(\text{sgn}(\beta_{\text{AWA}})\cos(\beta_{\text{AWA}})F_{l,a} + \sin(\beta_{\text{AWA}})F_{d,a}\right) \end{aligned} \tag{9}$$

for the aerodynamic force and, similarly, for the hydrodynamic force by

$$\begin{aligned} F_{f,h} &= \sin(\lambda)F_{l,h} - \cos(\lambda)F_{d,h} \\ F_{s,h} &= \cos(\lambda)F_{l,h} + \sin(\lambda)F_{d,h} \end{aligned} \tag{10}$$

In this projection, a negative sideways force should be interpreted as directed towards port while a positive sideways force is directed towards starboard. It follows that

$$\begin{aligned} F_{f,a} + F_{f,h} &= 0 \\ F_{s,a} + F_{s,h} &= 0 \end{aligned} \tag{11}$$

at steady-state. An illustration of the steady-state case can be obtained by combining Figs. 2–4, where $\vec{F}_a + \vec{F}_h = \vec{0}$.

In order to illustrate the projections, the use of the sign function, $\text{sgn}(\beta_{\text{AWA}})$ and lift and drag in general, the aerodynamic and hydrodynamic forward and sideways forces are illustrated in Fig. 6. The aerodynamic projections are illustrated as a function of apparent wind angle while the hydrodynamic projections are illustrated as a function of leeway. The figure is based on the sail, keel and hull of ASPire and calculated for a constant apparent wind speed of 5 m/s, a constant boat speed of 1 m/s and a constant angle of the wingsail, i.e., aerodynamic angle of attack, of 12°. This gives constant aerodynamic lift and drag. The corresponding projections of the aerodynamic lift and drag using Eq. (9) are illustrated as functions of apparent wind angle and would be sinusoidal without the sign function. Leeway, on the other hand, also forms the hydrodynamic angle of attack and accordingly hydrodynamic lift and drag will vary with leeway as the figure reveals.

As the figure illustrates, identical aerodynamic forward and sideways forces can also be obtained for different apparent wind angles, e.g., the effect of apparent wind angle of approximately 50° cannot be distinguished from that of approximately -150° and an evaluation of numerical results might need to bear this in mind. A detailed numerical framework for exploring the model is presented next.

3 Exploring the basic model

A figure such as Fig. 6 might be useful for a basic understanding of the forces and projections involved, but of limited value from a practical sailing perspective. Since the point of sailing is to harness the wind for moving the boat, boat speed and, perhaps, leeway, achieved for different wind speeds and angles are key variables. This is also the basis for widely spread velocity prediction programs (VPPs), first introduced in 1975 by Kerwin for the purpose of developing handicap systems for regattas [6]–[7].

Given apparent wind speed and angle (and angle of attack for the wingsail), the model can accordingly be used to calculate boat speed and

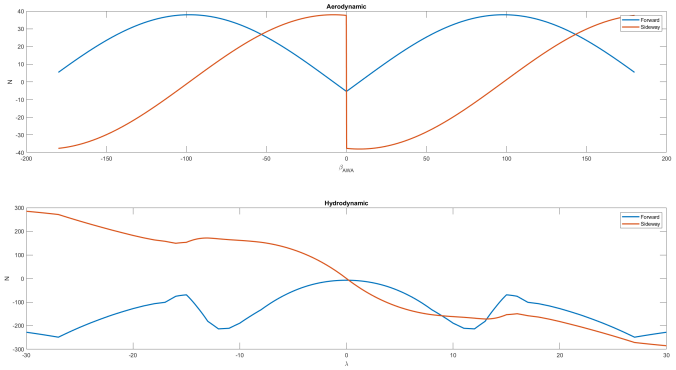

Figure 6: Upper panel: Projected aerodynamic forward (along the heading) and sideways (perpendicular to the heading) forces as a function of apparent wind angle. Lower panel: Projected hydrodynamic forward (along the heading) and sideways (perpendicular to the heading) forces as a function of leeway.

leeway by numerically solving Eq. (11). For later evaluation, it can be noted that for a given apparent wind angle, apparent wind speed and angle of attack for the wingsail, there might be zero, one or multiple solutions to the equation. This is illustrated in Figs. 7–10. Based on our static model, the stability of a solution cannot be determined, e.g., whether a solution appears only as a transient or not in a dynamic simulation. In the treatment that follows, we usually assume that the solution with higher boat speed corresponds to the expected stationary solution. This assumption is based on the narrow region of apparent wind angle for which the other solutions are obtained and also based on expected boat speed for a given wind. Unless mentioned, the solution corresponding to a higher boat speed is also used and illustrated in subsequent figures.

3.1 On-board perspective

Incidentally, the variables needed to calculate boat sped and leeway based on the model, i.e., apparent wind speed and angle (and angle of attack for the sail), are typically also measured on the boat. For clarity, we distinguish between this "on-board" perspective from the "on-shore" perspective based on true wind. In order to readily evaluate the performance, the expected boat speed and leeway predicted by the model for a constant angle of attack, $\alpha = 12°$, for Maribot Vane, as a function of apparent wind speed and angle are illustrated in Figs. 11–12.

In the polar plot where the apparent wind *direction* can be seen as fixed at zero degrees, i.e., a northerly wind, Fig. 12, it is natural to include leeway in the apparent wind angle, i.e., the angle in the plot is $\beta_{\mathrm{AWA},\lambda}$ and *not* β_{AWA}. This choice is made in order to illustrate the actual movement of the boat relative to the apparent wind. For point

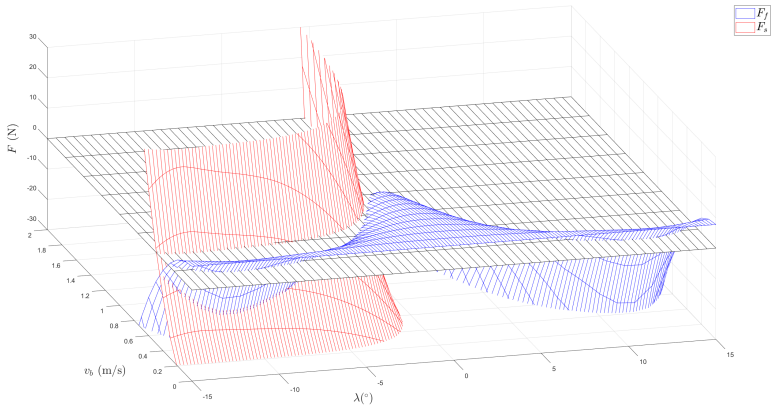

Figure 7: Forward and side-way forces, $F_{f,a} + F_{f,h}$ (blue) and $F_{s,a} + F_{s,h}$ (red), as functions of leeway, λ and boat speed v_b for an apparent wind angle, β_{AWA} of 20°. The zero-plane is included in black. Apparent wind speed, v_{AW}, is fixed at 5 m/s and angle of attack for the wingsail, α, at 12°. As seen, there are no solutions to Eq. (11).

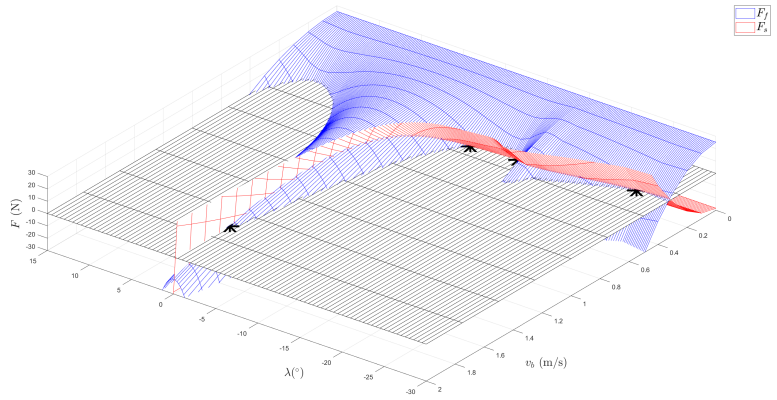

Figure 8: Same as in Fig. 7, but for an apparent wind angle, β_{AWA} of 50°. Four solutions to Eq. (11) are obtained, $v_b = 1.6$ m/s with $\lambda = -0.31°$, $v_b = 0.43$ m/s with $\lambda = -8.2°$, $v_b = 0.41$ m/s with $\lambda = -13°$ and $v_b = 0.33$ m/s with $\lambda = -26°$. The solutions are marked with black stars.

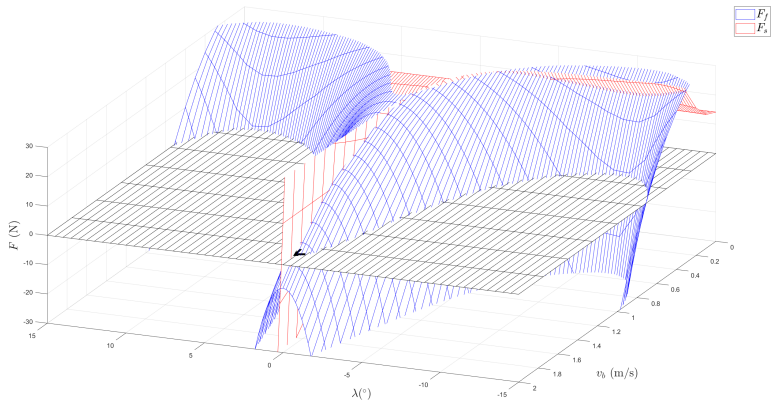

Figure 9: Same as in Fig. 8, but for an apparent wind angle, β_{AWA} of 120°. One solution to Eq. (11) is obtained, $v_b = 1.9$ m/s with $\lambda = 0.12°$.

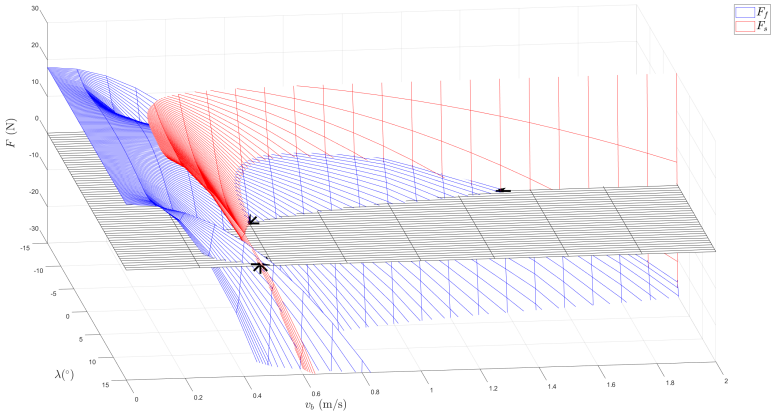

Figure 10: Same as in Fig. 8, but for an apparent wind angle, β_{AWA} of 160°. Three solutions to Eq. (11) are obtained, $v_b = 1.4$ m/s with $\lambda = 0.51°$, $v_b = 0.50$ m/s with $\lambda = 5.8°$ and $v_b = 0.46$ m/s with $\lambda = 15°$.

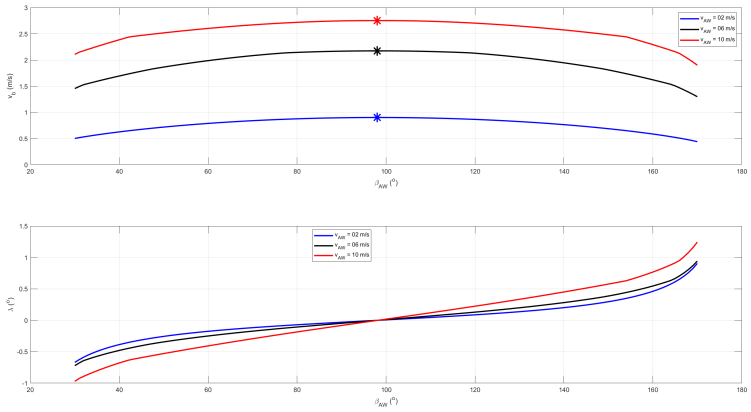

Figure 11: Boat speed v_b (upper panel) and leeway λ (lower panel) as a function of apparent wind angle β_{AWA} for three different apparent wind speeds v_{AW}. The highest boat speeds for each apparent wind speed are marked with stars.

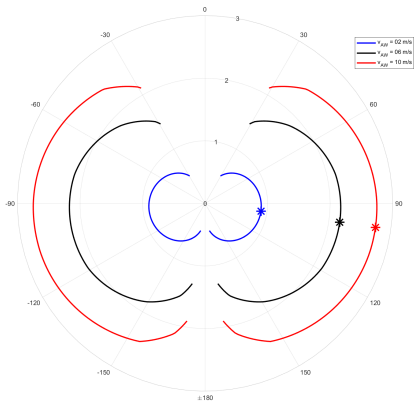

Figure 12: Polar plot of boat speed v_b as a function of apparent wind angle *including* leeway, $\beta_{\mathrm{AWA},\lambda}$ for three different apparent wind speeds v_{AW}. The highest boat speeds for each apparent wind speed are marked with stars.

of reference, the highest boat speeds for each apparent wind speed are marked with stars. As the figures reveal, the highest speeds are obtained for zero leeway. This corresponds to the special case that the sideways projection of the aerodynamic lift is cancelled by the sideways projection of the aerodynamic drag, i.e.,

$$\cos(\beta_{\mathrm{AWA}})F_{l,a} = -\sin(\beta_{\mathrm{AWA}})F_{d,a} \tag{12}$$

For a constant angle of attack for the wingsail, lift to drag is constant (the dependence of lift and drag on apparent wind speed is neglected), it follows that

$$\tan(\beta_{\mathrm{AWA}}) = -\frac{F_{l,a}}{F_{d,a}} = -\frac{C_l}{C_d} \tag{13}$$

which in the case of $\alpha = 12^\circ$ gives $\beta_{\mathrm{AWA}} \approx 98^\circ$. As a curiosity, it can be noted that for $\beta_{\mathrm{AWA}} > 98^\circ$ the boat is apparently pulled to leeward. This is discussed further in Section 6.

For someone familiar with VPPs, boat polar plots and yacht performance, the perspective illustrated in Fig. 12 might seem awkward. It is included in the current presentation on order to clarify the differences between an on-board and an on-shore perspective. A more "traditional" boat polar based on true wind is included in the next subsection.

3.2 On-shore perspective

In reality, a constant apparent wind speed for all apparent wind angles cannot be expected. Instead, it is reasonable to assume a constant *true* wind speed v_{TW} and true wind direction β_{TWD} and determine corresponding boat speeds for different true wind angles, β_{TWA} (or $\beta_{\mathrm{TWA},\lambda}$). This is also the traditional on-shore perspective typically used in books about sailing and for, e.g., mission planning. In order to incorporate true wind in the model, the geometry of the sailing velocity triangle, $\vec{v}_{\mathrm{TW}} = \vec{v}_{\mathrm{AW}} + \vec{v}_b$, illustrated in Fig. 2 is included in the model. When v_{TW} and β_{TWA} are provided, v_b can be determined as before with the law of cosines used to determine v_{AW} and β_{AWA} needed for the model.

That the results of Figs. 11–12 cannot easily be used to determine the corresponding boat speed for a constant true wind speed is illustrated well in Fig. 13. As can be noted, true wind speed would need to vary significantly in order to obtain a constant apparent wind speed when sailing at different angles towards the apparent wind, e.g., a $\pm 20\%$ variation in v_{TW} for $v_{\mathrm{AW}} = 10$ m/s. This has the effect that the highest sailing speeds are obtained at *smaller* true wind angles and not larger as the sailing velocity triangle and the upper panel of Fig. 13 would indicate. The expected performance for a constant true wind speed is illustrated in Figs. 14–15.

Before discussing further use and possible development, the basic model is evaluated on data from the two autonomous sailing robots.

4 Validating the basic model

For validating the basic model, eight sets of data collected with ASPire and Maribot Vane are used. ASPire (upper left) and Maribot Vane (upper

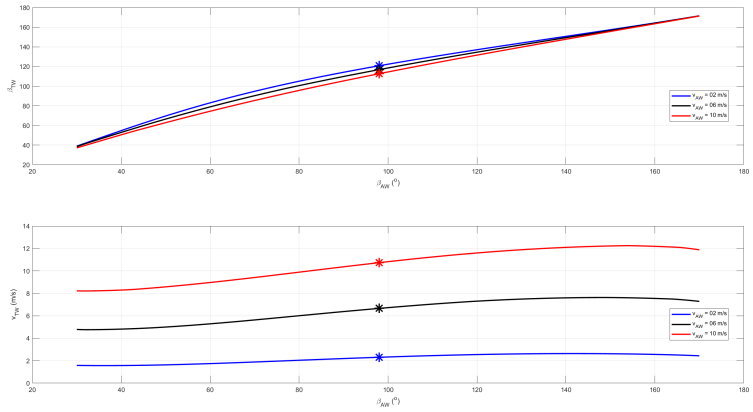

Figure 13: True wind angle β_{TWA} (upper panel) and true wind speed v_{TW} (lower panel) as a function of apparent wind angle β_{AWA} for three different apparent wind speeds v_{AW}.

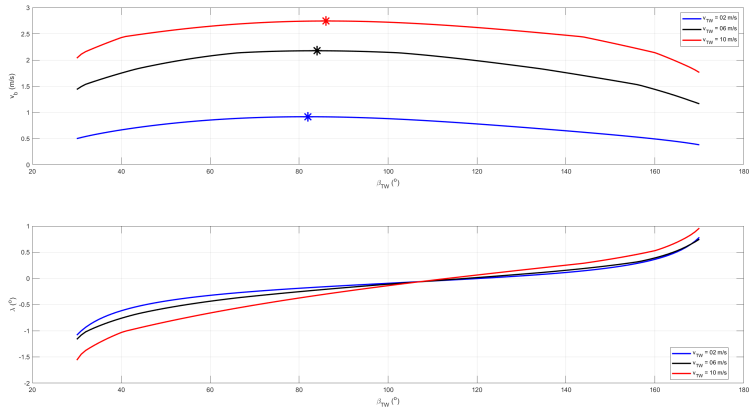

Figure 14: Boat speed v_b (upper panel) and leeway λ (lower panel) as a function of true wind angle β_{TWA} for three different true wind speeds v_{TW}. The highest boat speeds for each true wind speed are marked with stars.

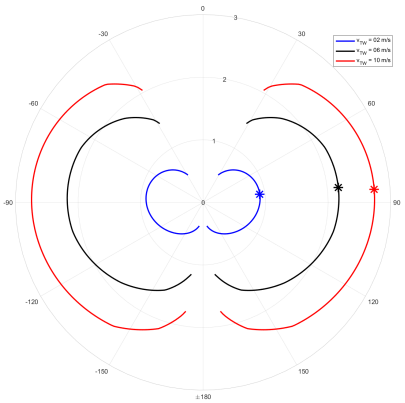

Figure 15: Polar plot of boat speed v_b as a function of true wind angle *including* leeway, $\beta_{\mathrm{TWA},\lambda}$ for three different true wind speeds v_{TW}. The highest boat speeds for each true wind speed are marked with stars.

right) along with two locations each for collecting sailing data are depicted in Fig. 16.

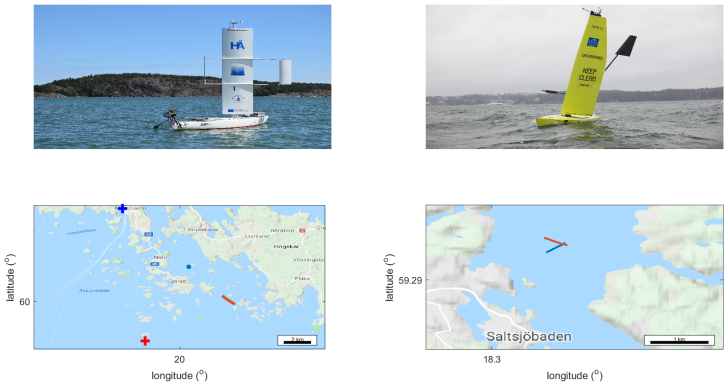

Figure 16: ASPire (upper left, © Anna Friebe) and Maribot Vane (upper right, © Ulysse Dhomé) and maps of sailing (lower panels). Lower left: ASPire datasets seen as blue dot and red line. Västra Hamnen (blue cross) and Nyhamn (red cross) are two Finnish Meteorological Institute weather stations. Lower Right: two of the datasets from Maribot Vane in blue and red).

4.1 Data from ASPire

Two different datasets collected with ASPire on June 12th, 2018 are used. The first set stretches over 30 seconds, marked with a blue dot in the lower left panel of Fig. 16, and the second set, collected about an hour later, stretches over 1000 seconds and is marked with a red line. The sailing waters are just south of mainland Åland in the middle of the Baltic Sea. The locations of the closest two official weather stations of the Finnish Meteorological Institute are indicated by a red cross (Nyhamn, Lemland) and a blue cross (Västra Hamnen, Mariehamn). Measurements of course, heading and apparent wind angle are illustrated as functions of time in the left panels of Fig. 17, upper for dataset 1 and lower for dataset 2. The right panels illustrate corresponding boat and apparent wind speed. ASPire is designed to sail with a constant angle of attack towards the apparent wind and since this angle was not continuously measured, the estimate $\alpha = 15^\circ$ used is based on visual inspection.

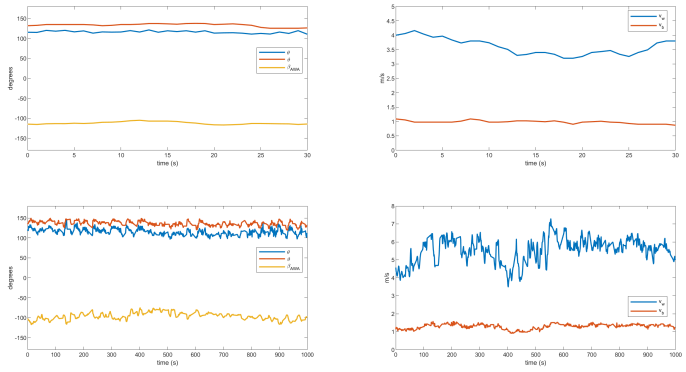

Figure 17: Left panels: heading (blue) with a mean value of 120° (upper) and 110° (lower), course (red) with a mean value of 130° (upper) and 140° (lower), apparent wind angle (yellow) with a mean value of -110° (upper) and -100° (lower). Right panels: wind speed (blue) with a mean value of 3.6 m/s (upper) and 5.5 m/s (lower) and boat speed (red) with a mean value of 1.0 m/s (upper) 1.3 m/s (lower).

Using data from the two weather stations indicated in Fig. 16 for the same time, three ten-minute averages with similar values indicate a true wind speed between 4.2 m/s (Nyhamn) and 5.5 m/s (Västra Hamnen) and a true wind direction of 34° (Nyhamn) and 337° (Västra Hamnen) for dataset 1. The measured apparent wind speed of 3.6 m/s and apparent wind direction between 4° (using measured heading) and 23° (using measured course) thus seem reasonable. Using four ten-minute averages, the official weather stations indicate a true wind speed between 5.4 m/s (Nyhamn) and 4.9 m/s (Västra Hamnen) and a true wind direction of 326° (Nyhamn) and 342° (Västra Hamnen). The measured apparent

wind speed of 5.5 m/s seems reasonable while the apparent wind direction between 19° (based on measured heading) and 40° (based on measured course) deviate slightly more, but can still be explained by local variations. While both sets are reasonable approximations of equilibrium, the second set is much longer and correspondingly contain larger variations. On average, the wind and boat speed are also significantly higher in the second set.

4.2 Data from Maribot Vane

For Maribot Vane, six sets of data collected on November 15$^{\text{th}}$, 2018, are studied. All sets last approximately 4 minutes each, and measurements of course, heading and apparent wind angle for two of the sets are illustrated as functions of time in the left panels of Fig. 18. Apparent wind speed and boat speed are depicted in the right panels. Observations recorded at the Stockholm station of the Swedish Meteorological and Hydrological Institute approximately 15 km to the west of the sailing waters provide a mean true wind direction of 230° and a true wind speed of 4 m/s of which at least the latter is consistent with the collected data. Two of the sailing routes are depicted in the lower right panel of Fig. 16. In addition, a measurement of the angle of attack of the wingsail can be used.

Interestingly, and in contrast to the data collected with ASPire, different tacks, and different headings can be noted in the sets. The data could thus also have the potential to either confirm or reject the existence of a (stable) current. As Fig. 18 illustrates for two different sets of data, there are also, depending on the data, some variations in apparent wind speed and boat speed. Strictly taken, these observed changes correspond to a deviation from the assumption of equilibrium but are assumed to not significantly effect the results.

The measured angle of attack for Maribot Vane indicated significantly different angles of attack depending on whether sailing on a port or starboard tack. Telltales were used to visually confirm that that airflow was not stalled and for this reason the angle of attack was limited to $\alpha = 15°$ for the analysis that follows, despite some measurements indicating $\alpha = 21°$.

4.3 Basic validation

For a basic validation of the model, the boat speeds expected based on measurements of apparent wind speed, apparent wind angle and measurements (or estimates) of angle of attack for the wingsails are determined. These are provided in Table 3.

An average relative error for boat speed, $r_E = \frac{|v_b - \hat{v}_b|}{v_b}$, of 15% for Maribot Vane and 52% for ASPire can be noted. Estimated boat speeds are all higher than actual measurements and the bias of the model can, at least in part, be due to simplifications discussed in connection to Section 6. Still, the results for Maribot Vane are encouraging and the results seem useful for performance evaluation and monitoring. The larger mismatch in boat speed noted for ASPire could also indicate poorer trim which in itself might be a consequence of the challenges encountered with the

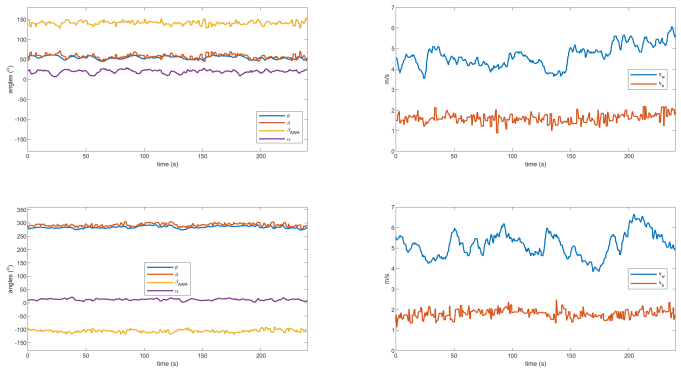

Figure 18: Left panels: heading (blue) with a mean value of 54° (upper) and 280° (lower), course over ground (red) with a mean value of 58° (upper) and 290° (lower), apparent wind angle (yellow) with a mean value of 130° (upper) and -110° (lower), mean wingsail angle of attack of 20° (upper) and 12° (lower). Right panels: apparent wind speed (blue) with a mean value of 4.7 m/s (upper) and 5.2 m/s (lower), boat speed (red) with a mean value of 1.6 m/s (upper) and 1.8 m/s (lower).

$\theta(^\circ)$	$\vartheta(^\circ)$	$\beta_{\mathrm{AWA}}(^\circ)$	v_{AW} (m/s)	$\alpha(^\circ)$	v_b (m/s)	$\hat{v_b}$ (m/s)	$\lambda(^\circ)$	$\hat{\lambda}(^\circ)$	R_F (N)
116.0	133.3	-112.0	3.6	15.0	1.0	*1.5*	-17.3	*-0.0*	9.8
114.9	136.3	-95.8	5.5	15.0	1.3	*2.0*	-21.4	*0.1*	9.4
248.2	258.4	-63.8	5.4	10.7	1.6	*1.9*	-10.2	*0.2*	15.1
54.4	57.7	141.3	4.7	15.0	1.6	*1.6*	-3.3	*0.2*	7.9
154.7	161.8	35.8	6.2	15.0	1.0	*1.3*	-7.1	*-0.9*	3.4
283.9	292.5	-105.8	5.2	12.2	1.8	*1.9*	-8.6	*-0.0*	17.6
113.0	119.4	80.6	6.6	15.0	1.8	*2.2*	-6.4	*-0.2*	8.9
321.9	327.6	-142.0	3.9	10.3	1.2	*1.4*	-5.7	*-0.2*	9.2

Table 3: Measurements (in black) and estimates (italics in blue). Values for the measure of mismatch between model and data, R_F introduced in Eq. (14), determined based on measurements are for reference included in the last column. Data from ASPire on the first two rows and data from Maribot Vane on the other six rows.

design of the wingsail. Iterative adjustments of the design led, in turn, to challenges with the weight distribution. A significant mismatch in itself can thus also be an indicator of possibilities for improvement in design.

Although sailing performance as quantified by boat speed is central for any analysis, this "VPP-perspective" is not the only possibility. Indeed, the significantly higher discrepancy between model and measurements for leeway noted in Table 3 might warrant a more general model evaluation. This, with some alternatives that also form the basis for an approach for model-based fault detection, is presented next.

5 Model-based data assessment

In this section, an approach for fault-diagnosis that uses the basic model is introduced. Although perhaps most useful for initial evaluations of pilot projects, it can also be useful for general monitoring and a valuable complement to purely statistical methods.

5.1 Consistency check

Since $\vec{F}_a = \vec{F}_h$ at equilibrium, i.e., Eq. (11) holds, an initial screening of data can be achieved by calculating

$$R_F = \sqrt{\frac{F_{l,h}^2 + F_{d,h}^2}{F_{l,a}^2 + F_{d,a}^2}} \tag{14}$$

The use of the square root is motivated by the possible use of models for real-time monitoring of forces. Ideally, R_F should be equal to one and significant deviations indicate an inconsistency between data and model. Attempting to explain an observed inconsistency requires a more detailed analysis presented next.

5.2 Detailed data analysis

Given the two nonlinear equations of Eq. 11, several possibilities for exploring their dependence on the five (measured) variables, leeway[1], apparent wind angle, apparent wind speed, boat speed and angle of attack for the wingsail, could be conceived. Given that we are interested in exploring the mismatch between measured data and model, we first consider a general configuration of using three measurements and solving Eq. 11 to provide estimates of the remaining two. For reference and an improved understanding, these results are given in Appendix A.

Summarizing the results presented in the Appendix, it can be noted that as long as leeway is one of the estimated variables, i.e., Tables 4–7, reasonable solutions to Eq. 11 are obtained simply with a slightly smaller apparent wind speed (Table 6), smaller boat speed as noted earlier (Table 4), or even with a different angle of attack for the wingsail (Table 7).

If, on the other hand, measured leeway is considered correct, three basic alternative explanations can be noted:

1. rather easily rejected solutions such as almost no wind and consequently almost no boat speed, i.e., Table 9,
2. alternative solutions discussed in connection to Figs. 7–10 with a low boat speed compared to the apparent wind speed, i.e., Tables 11 and 8, and
3. (almost) no solutions at all, Tables 10 and 12–13.

[1] In practice, leeway is typically calculated based on measured heading and measured course over water. The model depends only on leeway and not absolute values for heading and course over water and therefore only leeway can be evaluated with respect to the model.

If the solutions with significantly lower boat speeds are considered unlikely, or unstable as discussed earlier, the main difference between model and measurements is in leeway. Some implications of this observation are discussed in the next section.

As an alternative, it can be questioned whether it is advisable to exactly satisfy Eq. (11). The model includes simplifications that render the equations approximate at best. For example, even under ideal conditions the coefficients C_l and C_d are not exactly known and may vary with time and use, the wind around the sail is not necessarily uniform and constant, mechanical inaccuracies can include twist and asymmetries, measurements and assumption of equilibrium are only approximate, etc. Therefore, it could be valuable to estimate only one of the five variables and assess the possible improvement in consistency between measurements and model thus obtained. In the general case, it will not be possible to solve Eq. (11) by varying one variable only. Instead, we suggest minimizing

$$V(x) = c(F_{f,a} + F_{f,h})^2 + (1-c)(F_{s,a} + F_{s,h})^2 \tag{15}$$

with respect to x where x is, in turn, one of the five variables considered. The parameter c, $0 \leq c \leq 1$, can be used to emphasize either forward or sideways balances.

For comparing the results, $V_0(x)$ is used to denote the value obtained with no minimization, i.e., measurements are used for all variables. A value for $1 - V(x)/V_0(x)$ of one thus indicates a perfect fit to data while a value close to zero indicates that little improvement in the fit can be obtained by optimizing Eq. (15). Results with $c = 0.5$, i.e., no emphasis on any term, are provided in Tables 14–18. Since Eq. (15) might have several local minima there is no guarantee that the global minimum has been found, but several random initial values for the numerical routines were explored.

Summarizing the results presented in the Tables, the discrepancy between model and data is almost eliminated by setting leeway very small (Table 14) or by significantly decreasing boat speed (Table 14). In some cases, an improved fit can be obtained with a significantly higher apparent wind speed (Table 17). Finally, very little improvement in the fit can be obtained by varying apparent wind angle (Table 16) or angle of attack for the wingsail (Table 18).

5.3 Model-based fault diagnosis

Summarizing the analysis presented in the previous Section, the most significant discrepancy between measurements and model is in leeway, regardless of whether Eq. 11 is solved or Eq. (15) is minimized. This provides support for four possible explanations:

1. Heading measurements are unreliable.
2. Measurements of course over ground are unreliable.
3. Measurements of course over ground do not correspond to course over water.
4. The model underestimates leeway.

Concerning the last explanation, some simplifications included in the model and possibilities for model development are discussed in the next section. If, for now, the model is deemed reliable, this leaves the other three explanations. With consistent speed and connected to a sufficient number of satellites, GPS measurements of speed and course over ground are usually very reliable. Therefore, a reasonable conclusion from the numerical analysis is that either the measurements of heading are unreliable or there is a current that can explain why course over ground does not equal course over water. An estimate of such a current is provided in Table 19. For the data from ASPire, the direction of the current is quite consistent but not so for Maribot Vane. For all sets of data, the speed of the currents that would be needed to explain the leeway is highly unlikely in these waters and contrary to observations during the experiments. The analysis does, however, provide support for the use of independent sensors for measuring speed (and direction) over water.

For ASPire, a similar conclusion for both data-sets can accordingly be established: the analysis of data consistently implies unreliable measurements of heading. Indeed, the presence of electromagnetic disturbances was later noted and the compass-unit subsequently moved. The approach thus seems promising for automating (some) fault detection and diagnosis. Had the approach of this paper been applied at an early stage, the unreliability of the compass-unit had also been noted and addressed. This, in turn, could have provided more reliable data and a more advantageous basis for improved control design and model development.

Despite some quite significant differences between the six sets of data from Maribot Vane, the same conclusion stands: Measured heading does not agree with the model. Also, measured leeway is consistently negative for all sets which is contrary to expected behavior considering the different points of sailing during the experiment. For Maribot Vane, earlier trials revealed an unreliable compass which was replaced before collecting the data studied in the present paper. Although the replacing compass would also seem to be unreliable, an alternative can be considered. The alternative, if all measurements are reliable, is that the model does not adequately capture the leeway. In this case, the approach of the current paper indicates that the main deficit of the present model is that it does not explain the leeway experienced in practical experiments. An exploration of this possibility is provided next.

6 Model development

One of the main goals of this paper is to illustrate the basic physics of sailing for a rigid-wing sailboat in a few pages. For this reason the model has been kept simple, but shown to capture relevant features and be useful as a model-based approach to fault-detection. It was, however, seen that the measurements indicate larger leeway than the model would predict. Although inaccurate heading measurements are a likely explanation, a reevaluation of some simplifications included in the model seems justified. Some simplifications included are:

- the limitation to two dimensions, i.e., no heeling,

- no moment on the boat is generated by either the sail or the keel, i.e., no active rudder,
- no other aerodynamic forces, e.g., no hull over water, etc.

Of these simplifications, the last two are likely to make the model biased towards a smaller leeway. In addition, the effect of external waves, has, among other uncertainties and disturbances difficult to measure, been neglected in the data assessment.

An active rudder would decrease the lift of the keel while adding drag. Numerically, it was confirmed that decreasing the lift of the keel by 10 % increases the magnitude of the leeway by approximately 10 % at a true wind angle of 50° and 150°. For true wind angles between 50° and 150° the increase is smaller, and for slightly larger outside the region.

Changing the lift of the keel does not affect the equations involved in the model, and it could accordingly be considered a parametric change. Similarly, changing angle of attack for the wingsail, coefficients of lift and drag, geometry of sail, keel and hull, etc., can also be considered *parametric* changes. Changes in the model that cannot be captured simply by changing a parameter in the equations, on the other hand, could be considered *structural*. For example, if the hull over water is included and modeled as another rigid wing, this will add a different term to the equations for aerodynamic lift and drag. In this case, lift and drag from hull over water, $F_{l,b}$ and $F_{d,b}$, will also be included in the forward and sideways projections of the aerodynamic forces.

$$\begin{aligned} F_{f,a} &= \operatorname{sgn}(\beta_{\text{AWA}}) \sin(\beta_{\text{AWA}})(F_{l,a} + F_{l,b}) - \cos(\beta_{\text{AWA}})(F_{d,a} + F_{d,b}) \\ F_{s,a} &= -\left(\operatorname{sgn}(\beta_{\text{AWA}}) \cos(\beta_{\text{AWA}})(F_{l,a} + F_{l,b}) + \sin(\beta_{\text{AWA}})(F_{d,a} + F_{d,b})\right) \end{aligned} \tag{16}$$

In this case, aerodynamic lift and drag will no longer be constant despite a constant angle of attack for the wingsail since the angle of attack for the *hull* varies with the apparent wind angle β_{AWA}.

For simplicity, the same data for C_l and C_d as for the wingsail is used and the coefficients for lift and drag for the hull are (incorrectly) assumed to be symmetric around 90°, e.g., $C_l(x) = C_l(180^\circ - x)$ for $90^\circ < x < 180^\circ$. With the length of the hull at four meters and a height of 30 cm above water, the resulting boat speed and leeway as a function of true wind angle is provided in Fig. 19. For comparison, the figure includes the results using the basic model as dashed lines. As the figure reveals, the inclusion of hull-over-water does not significantly affect top boat speed, but the angle at which the top speed is achieved is slightly larger. The change in leeway, on the other hand, reveals a significantly larger drift. The larger leeway corresponds better to typical values less than 10° reported in the literature [5], but still not close to explaining measurements of heading. It can also be noted that with hull-over-water included in the model, the lift generated by the wingsail can no longer pull the boat to windward for larger true wind angles and the drift will, for all angles, be to leeward which is, perhaps, more in line with the expected behaviour.

In order to illustrate how the model can be used for quantifying improved performance by changing the design, Fig. 20 can serve as an exam-

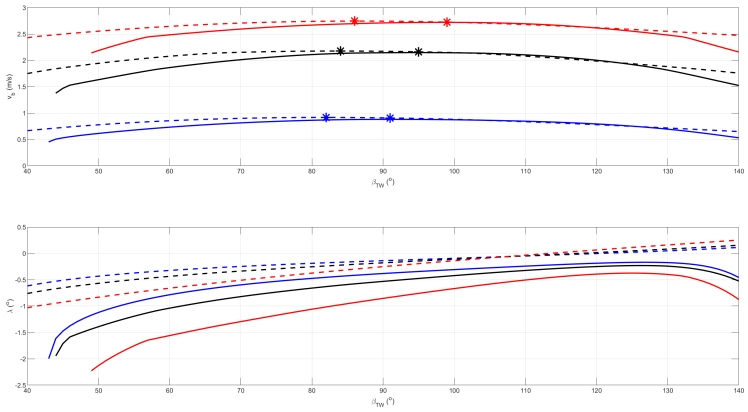

Figure 19: Boat speed v_b (upper panel) and leeway λ (lower panel) as a function of true wind angle β_{TWA} for three different true wind speeds v_{TW}, 2 m/s (blue), 6 m/s (black) and 10 m/s (red). The dashed lines illustrate v_b and λ for the basic model (same as in Fig. 14) while the solid lines include hull-over-water, i.e., Eq. (16). The highest boat speeds for each true wind speed are marked with stars (upper panel).

ple. The figure illustrates what can, according to the model, be achieved by enabling an arbitrary angle of attack for the wingsail. As expected for this type of sailboat, the optimal choice for maximizing boat speed transitions from primarily using lift at smaller (apparent) wind angles towards using drag. With the numerical framework applied in this paper, the added complexity of controlling and optimizing the angle of attack can thus easily be assessed against improved performance.

To summarize, the simple model and the comprehensive numerical framework introduced can be used a reference for quantifying model development, structural as well as parametric, by exploring the effect of uncertain parameters and possible improvements in design. For more exhaustive numerical investigations, it might be worthwhile to explore changes in several variables simultaneously given the nonlinear nature of the model. For such an exploration, it can be of numrical significance to keep in mind that the scales of the variables can differ significantly. Also, it can be noted that the characteristics of high-performing hydrofoil sailboats might be captured even better by the simple model since different terms for lift and drag dominate when F_{wave} and C_R in Eq. (6) can be set to zero.

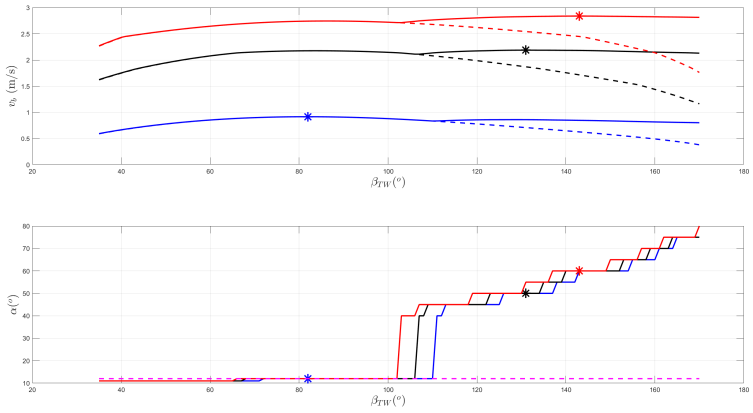

Figure 20: Boat speed v_b (upper panel) and angle of attack for the wingsail α (lower panel) as a function of true wind angle β_{TWA} for three different true wind speeds v_{TW}, 2 m/s (blue), 6 m/s (black) and 10 m/s (red). The dashed lines in the upper panels illustrate v_b for a constant angle of attack (same as in the upper panel of Fig. 14) while the solid lines illustrate v_b (upper panel) with the corresponding optimal choice of α (lower panel), i.e., the choice that will given the highest boat speed for a given (true) wind speed and (true) wind angle. The constant angle of attack $\alpha = 12^\circ$ used for the dashed lines is included in the lower figure. The highest boat speeds for the optimal choice of α for each true wind speed are marked with stars.

7 Conclusions

Using Newton's laws and (some) geometry, the basic physics behind sailing was presented in a simple model combined with a computational strategy for numerical evaluation. In detail, the differences in perspectives between on-shore planning and design on the one side, and on-board evaluation on the other, were presented. The basic steady-state model was evaluated on data from two rigid-wing sailing robots and found to predict sailing speed with reasonable accuracy. Furthermore, the approach was shown to be very useful as a tool for monitoring performance, detecting unreliable sensors, evaluating changes in design and assessing model development. Also, by estimating different forces acting on the sailboat the approach can provide a beneficial perspective for improving the robustness of the design, control and path-planning algorithms, e.g., choosing routes and strategies in real time that will put less strain on the vessel. As such, the approach should be of general interest for the design and development of rigid wing sailing robots.

References

[1] `https://www.walleniusmarine.com/our-services/ship-design-newbuilding/ship-design/wind-powered-vessels/`. [Online; accessed 30-September-2021]. 2021.

[2] U. Dhomé et al. "Development and initial results of an autonomous sailing drone for oceanic research". In: *Marine Design XIII – Proceedings of the 13th International Marine Design Conference*. Vol. 1. 2018. Chap. 60.

[3] F. Fossati. *Aero-Hydrodynamics and the Performance of Sailing Yachts*. London: Adlard Coles Nautical, 2009.

[4] A. Friebe et al. "A marine research ASV utilizing wind and solar power". In: *OCEANS 2017*. Aberdeen, 2017, pp. 1–7. DOI: `10.1109/OCEANSE.2017.8084648`.

[5] R. Garrett. *The Symmetry of Sailing — The Physics of Sailing for Yachtsmen*. London: Adlard Coles, 1987.

[6] J. E. Kerwin. *A Velocity Preiction Program for Ocean Racing Yachts*. Tech. rep. 75-17. Cambridge: Massachusetts Institute of Technology, 1975.

[7] J. E. Kerwin. *A Velocity Preiction Program for Ocean Racing Yachts*. Tech. rep. 78-11. Cambridge: Massachusetts Institute of Technology, 1978.

[8] R.E. Sheldahl and P.C. Klimas. *Aerodynamic Characteristics of Seven Symmetrical Airfoil Sections through 180-Degree Angle of Attack for Use in Aerodynamic Analysis of Vertical Axis Wind Turbines*. Tech. rep. Albaquerque: Sandia National Labs, 1981.

[9] M. F. Silva et al. “Rigid Wing Sailboats: A State of the Art Survey”. In: *Ocean Engineering* 187 (2019), pp. 1–20. DOI: 10.1016/j.oceaneng.2019.106150.

A Detailed data analysis—Tables

$\lambda(^\circ)$	v_b (m/s)	$\beta_{\text{AWA}}(^\circ)$	v_{AW} (m/s)	$\alpha(^\circ)$
-0.0	*1.5*	-112.0	3.6	15.0
0.1	*2.0*	-95.8	5.5	15.0
0.2	*1.9*	-63.8	5.4	10.7
0.2	*1.6*	141.3	4.7	15.0
-0.9	*1.3*	35.8	6.2	15.0
-0.0	*1.9*	-105.8	5.2	12.2
-0.2	*2.2*	80.6	6.6	15.0
-0.2	*1.4*	-142.0	3.9	10.3

Table 4: Measurements (in black) with estimates of λ and v_b (italics in blue). First two rows are data from ASPire, the rest from Maribot Vane.

$\lambda(^\circ)$	v_b (m/s)	$\beta_{\text{AWA}}(^\circ)$	v_{AW} (m/s)	$\alpha(^\circ)$
-0.5	1.0	*-173.3*	3.6	15.0
0.7	1.3	*-38.4*	5.5	15.0
0.4	1.6	*-42.7*	5.4	10.7
0.2	1.6	*145.3*	4.7	15.0
-1.6	1.0	*29.5*	6.2	15.0
0.2	1.8	*-63.2*	5.2	12.2
-0.5	1.8	*50.3*	6.6	15.0
-0.4	1.2	*-155.3*	3.9	10.3

Table 5: Measurements (in black) with estimates of λ and β_{AWA} (italics in blue). First two rows are data from ASPire, the rest from Maribot Vane.

$\lambda(^\circ)$	v_b (m/s)	$\beta_{\text{AWA}}(^\circ)$	v_{AW} (m/s)	$\alpha(^\circ)$
-0.0	1.0	-112.0	*2.2*	15.0
0.0	1.3	-95.8	*3.2*	15.0
0.2	1.6	-63.8	*4.5*	10.7
0.2	1.6	141.3	*4.5*	15.0
-0.7	1.0	35.8	*4.2*	15.0
-0.0	1.8	-105.8	*4.7*	12.2
-0.1	1.8	80.6	*5.1*	15.0
-0.2	1.2	-142.0	*3.4*	10.3

Table 6: Measurements (in black) with estimates of λ and v_{AW} (italics in blue). First two rows are data from ASPire, the rest from Maribot Vane.

$\lambda(^\circ)$	v_b (m/s)	$\beta_{\text{AWA}}(^\circ)$	v_{AW} (m/s)	$\alpha(^\circ)$
-0.1	1.0	-112.0	3.6	*3.0*
-0.0	1.3	-95.8	5.5	*2.4*
0.2	1.6	-63.8	5.4	*5.6*
0.2	1.6	141.3	4.7	*13.5*
-1.5	1.0	35.8	6.2	*17.2*
-0.0	1.8	-105.8	5.2	*7.5*
-0.1	1.8	80.6	6.6	*4.3*
-0.3	1.2	-142.0	3.9	*6.5*

Table 7: Measurements (in black) with estimates of λ and α (italics in blue). First two rows are data from ASPire, the rest from Maribot Vane.

$\lambda(^\circ)$	v_b (m/s)	$\beta_{\text{AWA}}(^\circ)$	v_{AW} (m/s)	$\alpha(^\circ)$
-17.3	*0.3*	*-164.1*	3.6	15.0
-21.4	*0.4*	*-160.6*	5.5	15.0
-10.2	*0.4*	*-137.7*	5.4	10.7
-3.3	*0.6*	*33.8*	4.7	15.0
-7.1	*0.6*	*52.7*	6.2	15.0
-8.6	*0.4*	*-144.5*	5.2	12.2
-6.4	*0.6*	*48.9*	6.6	15.0
-5.7	*0.4*	*-160.0*	3.9	10.3

Table 8: Measurements (in black) with estimates of v_b and β_{AWA} (italics in blue). First two rows are data from ASPire, the rest from Maribot Vane.

$\lambda(^\circ)$	v_b (m/s)	$\beta_{\text{AWA}}(^\circ)$	v_{AW} (m/s)	$\alpha(^\circ)$
-17.3	*0.0002*	-112.0	*0.0028*	15.0
-21.4	*0.0001*	-95.8	*0.0019*	15.0
-10.2	*0.0001*	-63.8	*0.0020*	10.7
-3.3	*0.0002*	141.3	*0.0048*	15.0
-7.1	*0.0000*	35.8	*0.0034*	15.0
-8.6	*0.0001*	-105.8	*0.0023*	12.2
-6.4	*0.0004*	80.6	*0.0045*	15.0
-5.7	*0.0009*	-142.0	*0.0098*	10.3

Table 9: Measurements (in black) with estimates of v_b and v_{AW} (italics in blue). First two rows are data from ASPire, the rest from Maribot Vane.

$\lambda(^\circ)$	v_b (m/s)	$\beta_{\text{AWA}}(^\circ)$	v_{AW} (m/s)	$\alpha(^\circ)$
-17.3	*NaN*	-112.0	3.6	*NaN*
-21.4	*NaN*	-95.8	5.5	*NaN*
-10.2	*NaN*	-63.8	5.4	*NaN*
-3.3	*0.9671*	141.3	4.7	*117.4885*
-7.1	*NaN*	35.8	6.2	*NaN*
-8.6	*NaN*	-105.8	5.2	*NaN*
-6.4	*0.8135*	80.6	6.6	*40.4291*
-5.7	*0.0000*	-142.0	3.9	*0.0887*

Table 10: Measurements (in black) with estimates of v_b and α (italics in blue). First two rows are data from ASPire, the rest from Maribot Vane. NaN means that no solution was found.

$\lambda(^\circ)$	v_b (m/s)	$\beta_{\text{AWA}}(^\circ)$	v_{AW} (m/s)	$\alpha(^\circ)$
-17.3	1.0	*49.9469*	*11.2544*	15.0
-21.4	1.3	*53.7785*	*17.0194*	15.0
-10.2	1.6	*-137.5566*	*21.1565*	10.7
-3.3	1.6	*34.4756*	*13.1014*	15.0
-7.1	1.0	*52.5021*	*11.3502*	15.0
-8.6	1.8	*-144.1916*	*21.6750*	12.2
-6.4	1.8	*49.5053*	*19.6090*	15.0
-5.7	1.2	*-160.0588*	*12.0018*	10.3

Table 11: Measurements (in black) with estimates of β_{AWA} and v_{AW} (italics in blue). First two rows are data from ASPire, the rest from Maribot Vane.

$\lambda(^\circ)$	v_b (m/s)	$\beta_{\text{AWA}}(^\circ)$	v_{AW} (m/s)	$\alpha(^\circ)$
-17.3	1.0	*NaN*	3.6	*NaN*
-21.4	1.3	*NaN*	5.5	*NaN*
-10.2	1.6	*NaN*	5.4	*NaN*
-3.3	1.6	*NaN*	4.7	*NaN*
-7.1	1.0	*NaN*	6.2	*NaN*
-8.6	1.8	*NaN*	5.2	*NaN*
-6.4	1.8	*NaN*	6.6	*NaN*
-5.7	1.2	*NaN*	3.9	*NaN*

Table 12: Measurements (in black) with estimates of β_{AWA} and α (italics in blue). First two rows are data from ASPire, the rest from Maribot Vane. NaN means that no solution was found.

$\lambda(^\circ)$	v_b (m/s)	$\beta_{\text{AWA}}(^\circ)$	v_{AW} (m/s)	$\alpha(^\circ)$
-17.3	1.0	-112.0	*NaN*	*NaN*
-21.4	1.3	-95.8	*NaN*	*NaN*
-10.2	1.6	-63.8	*NaN*	*NaN*
-3.3	1.6	141.3	*NaN*	*NaN*
-7.1	1.0	35.8	*NaN*	*NaN*
-8.6	1.8	-105.8	*NaN*	*NaN*
-6.4	1.8	80.6	*15.0*	*39.6*
-5.7	1.2	-142.0	*NaN*	*NaN*

Table 13: Measurements (in black) with estimates of v_{AW} and α (italics in blue). First two rows are data from ASPire, the rest from Maribot Vane. NaN means that no solution was found.

$\lambda(^\circ)$	$\hat{\lambda}(^\circ)$	v_b (m/s)	$\beta_{\text{AWA}}(^\circ)$	v_{AW} (m/s)	$\alpha(^\circ)$	$1 - V(x)/V_0(x)$	R_F
-17.3	*-0.0497*	1.0	-112.0	3.6	15.0	*0.9955*	*0.4*
-21.4	*-0.0000*	1.3	-95.8	5.5	15.0	*0.9943*	*0.3*
-10.2	*-0.0000*	1.6	-63.8	5.4	10.7	*0.9982*	*0.6*
-3.3	*-0.0000*	1.6	141.3	4.7	15.0	*0.9954*	*0.8*
-7.1	*-1.6438*	1.0	35.8	6.2	15.0	*0.9985*	*1.0*
-8.6	*-0.0484*	1.8	-105.8	5.2	12.2	*0.9999*	*0.8*
-6.4	*-0.2505*	1.8	80.6	6.6	15.0	*0.9981*	*0.7*
-5.7	*-0.3341*	1.2	-142.0	3.9	10.3	*0.9995*	*0.9*

Table 14: Measurements (in black) and, with respect to Eq. (15), optimal value for λ (italics in blue). The fit to the data given by $1 - V(x)/V_0(x)$ and by the measure of mismatch given by Eq. (14), R_F, are provided in the last two columns (italics in blue). First two rows are data from ASPire, the rest from Maribot Vane.

$\lambda(^\circ)$	v_b	$\hat{v}_b$ (m/s)	$\beta_{\text{AWA}}(^\circ)$	v_{AW} (m/s)	$\alpha(^\circ)$	$1 - V(x)/V_0(x)$	R_F
-17.3	1.0	*0.2*	-112.0	3.6	15.0	*0.9926*	*0.6*
-21.4	1.3	*0.3*	-95.8	5.5	15.0	*0.9900*	*0.4*
-10.2	1.6	*0.2*	-63.8	5.4	10.7	*0.9958*	*0.3*
-3.3	1.6	*0.0*	141.3	4.7	15.0	*0.9854*	*0.0*
-7.1	1.0	*0.5*	35.8	6.2	15.0	*0.9861*	*1.0*
-8.6	1.8	*0.4*	-105.8	5.2	12.2	*0.9986*	*0.8*
-6.4	1.8	*0.6*	80.6	6.6	15.0	*0.9957*	*0.8*
-5.7	1.2	*0.4*	-142.0	3.9	10.3	*0.9986*	*0.9*

Table 15: Same as in Table 14 but with an optimal value for v_b.

$\lambda(^\circ)$	v_b (m/s)	$\beta_{\mathrm{AWA}}(^\circ)$	$\hat{\beta}_{\mathrm{AWA}}(^\circ)$	v_{AW} (m/s)	$\alpha(^\circ)$	$1 - V(x)/V_0(x)$	R_F
-17.3	1.0	-112.0	*-164.4*	3.6	15.0	*0.0901*	*9.8*
-21.4	1.3	-95.8	*-160.5*	5.5	15.0	*0.1322*	*9.4*
-10.2	1.6	-63.8	*-137.6*	5.4	10.7	*0.0986*	*15.1*
-3.3	1.6	141.3	*34.5*	4.7	15.0	*0.2985*	*7.9*
-7.1	1.0	35.8	*52.5*	6.2	15.0	*0.0474*	*3.4*
-8.6	1.8	-105.8	*-144.2*	5.2	12.2	*0.0268*	*17.6*
-6.4	1.8	80.6	*-164.8*	6.6	15.0	*0.0396*	*8.9*
-5.7	1.2	-142.0	*-160.1*	3.9	10.3	*0.0132*	*9.2*

Table 16: Same as in Table 14 but with an optimal value for β_{AWA}.

$\lambda(^\circ)$	v_b (m/s)	$\beta_{\mathrm{AWA}}(^\circ)$	v_{AW} (m/s)	$\hat{v}_{\mathrm{AW}}$ (m/s)	$\alpha(^\circ)$	$1 - V(x)/V_0(x)$	R_F
-17.3	1.0	-112.0	3.6	*8.8*	15.0	*0.2921*	*1.6*
-21.4	1.3	-95.8	5.5	*11.1*	15.0	*0.1118*	*2.3*
-10.2	1.6	-63.8	5.4	*11.2*	10.7	*0.0470*	*3.6*
-3.3	1.6	141.3	4.7	*0.0*	15.0	*0.0816*	*2e10*
-7.1	1.0	35.8	6.2	*11.1*	15.0	*0.8424*	*1.0*
-8.6	1.8	-105.8	5.2	*19.2*	12.2	*0.5787*	*1.3*
-6.4	1.8	80.6	6.6	*18.1*	15.0	*0.6741*	*1.2*
-5.7	1.2	-142.0	3.9	*11.7*	10.3	*0.8809*	*1.1*

Table 17: Same as in Table 14 but with an optimal value for v_{AW}.

$\lambda(^\circ)$	v_b (m/s)	$\beta_{\mathrm{AWA}}(^\circ)$	v_{AW} (m/s)	$\alpha(^\circ)$	$\hat{\alpha}(^\circ)$	$1 - V(x)/V_0(x)$	R_F
-17.3	1.0	-112.0	3.6	15.0	*11.3*	*0.0347*	*9.3*
-21.4	1.3	-95.8	5.5	15.0	*11.1*	*0.0372*	*9.0*
-10.2	1.6	-63.8	5.4	10.7	*10.7*	*0.0000*	*15.1*
-3.3	1.6	141.3	4.7	15.0	*90.0*	*0.4256*	*3.5*
-7.1	1.0	35.8	6.2	15.0	*11.6*	*0.0794*	*3.2*
-8.6	1.8	-105.8	5.2	12.2	*11.4*	*0.0001*	*17.6*
-6.4	1.8	80.6	6.6	15.0	*15.8*	*0.0014*	*9.1*
-5.7	1.2	-142.0	3.9	10.3	*11.6*	*0.0042*	*9.0*

Table 18: Same as in Table 14 but with an optimal value for α.

$\theta(^\circ)$	$\vartheta(^\circ)$	$\beta_{\mathrm{AWA}}(^\circ)$	v_{AW} (m/s)	$\alpha(^\circ)$	v_b (m/s)	$\hat{v}_s$ (m/s)	$\hat{\varphi}(^\circ)$
116.0	133.3	-112.0	3.6	15.0	1.0	*0.6*	*87.1*
114.9	136.3	-95.8	5.5	15.0	1.3	*0.9*	*84.0*
248.2	258.4	-63.8	5.4	10.7	1.6	*0.4*	*201.8*
54.4	57.7	141.3	4.7	15.0	1.6	*0.1*	*-12.0*
154.7	161.8	35.8	6.2	15.0	1.0	*0.3*	*136.3*
283.9	292.5	-105.8	5.2	12.2	1.8	*0.3*	*223.8*
113.0	119.4	80.6	6.6	15.0	1.8	*0.4*	*85.0*
321.9	327.6	-142.0	3.9	10.3	1.2	*0.2*	*290.3*

Table 19: Measurements (black) and estimates (blue) of the speed, $\hat{v}_s$, and direction, $\hat{\varphi}$, (in earth frame) of a stream that could explain the measurements.